



Tuned layered double hydroxide-based catalysts inducing singlet oxygen evolution: Reactive oxygen species evolution mechanism exploration, norfloxacin degradation and catalysts screen based on machine learning

Dehai Yu ^{a,*}, Fei Wu ^b, Junguo He ^{c,*}, Langming Bai ^a, Yanshi Zheng ^a, Ziyao Wang ^a, Jie Zhang ^a

^a State Key Laboratory of Urban Water Resources and Environment, School of Environment, Harbin Institute of Technology, Harbin 150090, Heilongjiang, People's Republic of China

^b School of Water, Energy and Environment, Cranfield University, Cranfield, Bedfordshire, UK

^c School of Civil Engineering, Guangzhou University, Guangzhou 510006, Guangdong, People's Republic of China



ARTICLE INFO

Keywords:

Heterogeneous electro-Fenton
Density functional theory
Molecular dynamics simulation
Machine learning
Catalysts screening

ABSTRACT

Heterogeneous Electro-Fenton (Hetero-EF) is pursued as a booming technique for real effluent treatments. Here, a novel Simulation-Experiment-Prediction framework has been conceived to reveal atomic-level ROS evolution mechanisms and screen robust catalysts for Hetero-EF reaction. Dynamics-static calculations unveil that the spontaneous conversion pathway of $^1\text{O}_2$ generation, which elucidate the transformation from $^3\text{O}_2$, $^1\text{HO}_2$, $^3\text{O}_2$ to $^1\text{O}_2$, and confirm optimal $\text{Co}_3\text{Fe}_2\text{-LDH}$ catalysts with lowest rate-determining step and energy barrier (0.82 eV) of $^1\text{O}_2$ generation providing a reasonable and feasible strategy fabricating and tuning Hetero-EF catalysts for realistic contaminants. Subsequently, the $\text{Co}_3\text{Fe}_2\text{-LDH}$ was verified with best catalytic performance and $^1\text{O}_2$ yield, which increased by exceeding 20% on NFXN decay and the treatment time was shortened ~ 2 h. Machine learning establishes a Gradient Boosting Regressor model for exploring appreciable catalysts for environmental remediation. Our results inspired the exploration and application of quantum chemistry and artificial intelligence for environmental catalysis, remediation and real wastewater purification.

1. Introduction

Norfloxacin (NFXN) has been widely applied for bacterial infection treatment, which could easily inhibit the reproduction of plants, alters the microbial community structure, and finally influences human health. Therefore, it is imperative to treat NFXN pollutants, make them harmless and resourceful, and alleviate severe water pollution [1–4]. Heterogeneous electro-Fenton (Hetero-EF) processes have been proposed for robust removal performance and thorough mineralization of refractory organics [5–11], which used various solid catalysts in solution or anchored on the cathode [12,13]. In the Hetero-EF processes, reactive oxygen species (ROS), such as $\cdot\text{OH}$, $\cdot\text{O}_2^-$, $^1\text{O}_2$ and high-valent metal-oxo species (Fe^{IV} and Co^{IV}) [14–16], are the possible dominated active substances for pollutants decay and environmental remediation. Although the Fenton reaction has a long history in the environmental field, the reaction mechanisms, especially, the reciprocal transformations of multiple ROS on the surface of Hetero-EF catalysts are complicated and volatile. For example, $\cdot\text{OH}$ could be converted into

$\cdot\text{HO}_2$ and then transferred to $^1\text{O}_2$ via the deprotonation reaction in neutral aqueous by the Haber-Weiss circle [17]. Otherwise, the predominant ROS of the Hetero-EF process is $\cdot\text{OH}$, which merely produces from the Haber-Weiss process in an acid environment [18]. It is still fully challenging to understand the transformation mechanism of ROS in the Hetero-EF process through only advanced experimental technique or theory simulation. Meanwhile, to enhance the contaminant degradations and ROS generations performance, ascertaining the mechanisms and pathways of the ROS evolution is an urgent and essential work for environmental engineers.

In the past several years, density functional theory (DFT) calculation and molecular dynamics (MD) simulations have become feasible and efficient strategies for catalytic mechanism analysis, robust catalysts modification and phenomena explorations [19–22], etc. The emulation process simplifies the complicated experiments, offers a clarified catalyst optimization direction and enhances efficiency. Interestingly, it has been rarely reported that modified catalysts could induce manifold ROS for pollutant degradation and improve the Hetero-catalysis activities in

* Corresponding authors.

E-mail addresses: yuysqy@gmail.com (D. Yu), junguohe@263.net (J. He).

environmental catalysis [23–26]. Hence, it is indispensable operating the DFT and MD simulation to propose guidance directionally modifying the environmental catalysts and verifying the inherent characteristic in the Hetero-EF catalysis performance, which could provide guidelines for popularization and practical application of Hetero-EF technology.

Machine learning (ML) has been employed to design highly efficient materials for the energy storage and conversion process [27–34] and the catalytic activity of dual-metal-site and single-atom catalysts [22,35]. However, ML researches on Hetero-EF catalysts for ROS generation and refractory organic matter abatement are lacking, and in our opinion, this booming technique will be indeed valuable for this purpose. Simultaneously, ML-assisted materials design strategy with higher efficacy, shorter time and lower cost could also address some shortcomings of traditional experimental selection. Therefore, it is valuable and feasible to rapidly screen target catalysts, effectively optimize the experimental process and extend to engineering application.

Herein, a novel Simulation-Experiment-Prediction (SEP) framework is conceived to reveal the atomic-level mechanisms of ROS evolution reactions and to screen the robust catalysts for Hetero-EF reaction. The main objectives of this study are: 1) to further determine the radical or non-radical pathway of ROS evolution existed in the CoFe-layered double hydroxides-based (CoFe-LDH-based) catalysis process at the atomic level using static and dynamic dual-mode simulation; 2) to propose a feasible modified and tuned strategy for enhancing the catalysts performance and guide its optimization process; 3) to tune LDH catalysts based on the simulation, identify the influence of material fingerprints on pharmaceuticals removal and ROS generation performance tested by the probe, and evaluate the potential contribution of each ROS in the Hetero-EF process for pollutant degradation experimentally; 5) to develop a credible ML prediction model for selecting potent Hetero-EF catalysts.

2. Materials and methods

2.1. The fabrication of hetero-EF catalysts

Different fingerprint CoFe-LDH catalysts were chosen for the Norfloxacin (NFXN) degradation in the Hetero-EF process, in which the fingerprint of the LDH materials could easily be tuned by changing the transition metal ratio resulting in the diverse stoichiometric attributes, elemental properties, electronic structure and also other features. A one-step facile hydrothermal method was applied to prepare different fingerprints CoFe-LDH functional cathode [36–38]. Furthermore, the detailed raw materials, fabrication methods and characterization of LDH catalysts are described in [Test S1](#).

2.2. Pollutant degradation and ROS evolution performance in hetero-EF process

The detailed information of the pharmaceutical degradation and ROS evolution performance of the Hetero-EF process could be referred to the [Test S2](#) in the [Supplementary material](#).

2.3. Static density functional theory calculation for ROS mechanism

Static-Dynamics simulations for ROS conversion mechanism were performed in the Vienna Ab Initio Simulation Package (VASP 5.4.4) [39–41] and CP2K/Quickstep [42]. The detailed information could be referred to the [Test S3](#) in the [Supplementary material](#).

2.4. Machine learning for efficient catalysts searching and selection

The evaluation factors for the decontamination of NFXN and objective features for machine learning prediction models should be ascertained before building the prediction models. All the parameters for different machine learning models were obtained from the previous

experiments in this work and the Materials Agnostic Platform for Informatics and Exploration (Magpie) [22,43], which was applied for attributes computing, the validation experiments performing and searches running for materials and their fingerprint messages. The degradation rate (%) of NFXN was chosen to reflect the NFXN degradation performance. Although the single factor as the evaluation criteria and target feature might probably be pursued as inaccurate results, yet the immediate target of the paper was to preliminarily search novel and feasible catalysts for drug decontamination with lower research cost and quicker primary screening than that using the traditional method such as artificial experiments or high throughput screening [44–46]. Therefore, it is feasible to take into account the most important feature for balancing the cost, efficiency and accuracy.

Over 130 attributes are shown in the [Text S4](#) in [Supplementary material](#), that include four discrepant categories [22,43,47,48].

3. Results and discussion

3.1. Dynamic-static DFT calculation for ROS evolution and conversion mechanism

3.1.1. Molecular dynamics simulation for ROS conversion mechanism

It is indispensable to establish a reasonable theoretical system unveiling the behavior of LDH surface under a realistic environmental catalytic solution, which not only could save cost and simplify experiment procedure, but also infer the mechanisms of environmental catalysis and guide the realistic environmental chemistry experiments. The work first performed ab initio molecular dynamics (AIMD) simulations at 300 K to reveal the conversion process of $^1\text{O}_2$ evolution in neutral aqueous on LDH surfaces. Dynamic simulation noted that oxygen species could spontaneously react with H_2O in the aqueous and the H atoms on the CoFe-LDH surface. Firstly, the temperature and potential energy equilibrium for the MD simulation of ROS evolution reaction were tested to ensure precise MD statistics ([Fig. S1](#)). After 3 fs the system reached the balance, the oxygen groups were catalyzed on the surface of CoFe-LDH with the H_2O molecules in the solution. From the AIMD simulation, the oxygen species continually interacted with the H atoms (H_2O) nearby. The dynamics illustrated that oxygen molecules on the catalyst's surface were metastable and were able to convert to superoxide radicals and singlet oxygens, which was of great significance for the physicochemical activation nature of the CoFe-LDH. The conversion of individual snapshots of O_2 , $\cdot\text{O}_2$ and $^1\text{O}_2$ from the trajectory was also exhibited in [Fig. 1](#). The mutual transformation among the oxygen species could be visually observed that the protonation of $^* \text{O}_2$ to $^* \text{HO}_2^-$, the deprotonation of the $^* \text{HO}_2^-$ to $^* \text{O}_2^-$ and the electron rearrangement of $^* \text{O}_2^-$ to $^1\text{O}_2$.

At ~ 4 ps, it could be observed that O_2 on the surface of the CoFe-LDH was catalyzed by the H atom, which was abstracted from H_2O nearby ([Movie 1](#)). The transition state $^* \text{HO}_2^-$ species, albeit a transient intermediate, was formed and ascribed to be non-negligible for superoxide radicals' generation. Moreover, the dehydrogenation of $^* \text{HO}_2^-$ to $^* \text{O}_2^-$ was also discerned in the spatiotemporal distribution of the AIMD simulation. At ~ 5.28 ps, $^* \text{HO}_2^-$ lost its H^+ due to the interaction of the adjacent OH^- group ([Movie 2](#)). $^* \text{O}_2$ to $^* \text{HO}_2^-$ and $^* \text{O}_2^-$ have all been confirmed in simulation. Although the internal electron rearrangement was hard to be observed directly during the AIMD trajectory, singlet oxygen could also yield after ~ 10 ps.

Since oxygen groups tended to undergo facile adsorption-induced catalysis changes and $^1\text{O}_2$ was difficult to figure out on the surface of LDH catalysts [49], it is essential to explore the bond length change of oxygen species during natural reaction conditions. Further verification of the oxygen species generation reaction was carried out by investigating the O-O in oxygen groups and $\text{O}_{\text{oxy}}-\text{H}$ (the bond between oxygen groups and H atoms in the system) pair. As depicted in [Fig. 1](#), the $\text{O}_{\text{oxy}}-\text{H}$ bond length range could be approximately classified into three parts: (i) 1.0–1.8 Å, in this part, O atoms and H atoms in the aqueous could

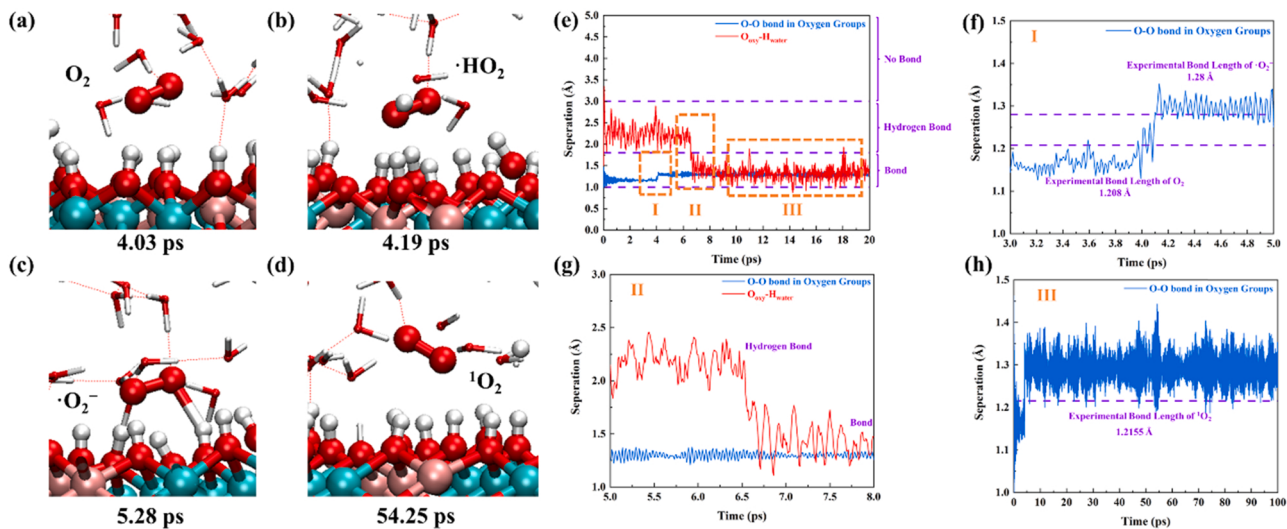


Fig. 1. Selected snapshots of the MD trajectory for Co₃Fe₂-LDH to show the ROS formation, oxygen (a), hydroperoxyl radical (b), superoxide radical (c), singlet oxygen (d), respectively. (e-h) The time evolution of the O-O bond in oxygen and O_{oxy}-H_{water} in the course of the AIMD simulation.

interact to form chemical bonds. The typical curve ranged after 7 ps in Fig. 1g; (ii) 1.8–3.0 Å, hydrogen atoms interact with O-O groups through the hydrogen bond, which was a typical covalent interaction in the solution. The covalent interaction was shown by the red trajectory from 0.0 to 6.5 ps. And the H bond could not be continuous for long. The H atoms could frequently and rapidly react with O atoms forming bonds and breaking bonds (As unveiled in snapshots, Fig. 1b, c), which is beneficial for the protonation reaction; (iii) > 3.0 Å, the distance between the O-H pair was too far to cause intense relation. (Exhibited in Fig. 1e).

As for the O-O bond in the groups, the separation between the O-O bond could intuitively mirror the O₂, ·O₂[−] to ¹O₂ generation process. In Fig. 1f, ranging from 3.0 to 5.0 fs, the blue trajectory directly exhibited the process that O₂ gained the electrons from LDH-based catalysts and H₂O in the aqueous to convert to ·O₂[−]. The O-O groups bond length ranged from ~1.208 to ~1.280 Å. After ~5 ps, the singlet oxygens, whose bond length is ~1.2155 Å (Fig. 1h) based on the experiment measurement, [50] were able to be obtained from their indispensable ·O₂[−] precursor.

To exert a more quantitative characterization of the ROS species evolution phenomenon, the radial distribution function (RDF) of O_{oxy}-H interaction was calculated shown in Fig. S2. In Fig. S2, there was a valley with negligible density between the first and second peaks, which verified that a strong O-H bond was formed. The phenomenon was consistent with the aforementioned snapshots and bond length change tracks analysis in the neutral solution. The first coordination layer contained 1 hydrogen atom and the distance of O atom and H atom was ~1.00 Å, which was pursued as the hydrogenation of *O₂ to *HO₂. The free energy diffusion barrier for the catalysis of *O₂ to *HO₂ was estimated by the mean force potential in Eq. (2). The estimated free energy barrier was merely 0.13 eV, which was obviously lower than the static DFT for O₂ activation (1.60 eV for Co₃Fe₂-LDH).

$$V(r) = -RT\ln(g(r)) \quad (2)$$

Where g(r) is the RDF of O_{oxy}-H bond.

These AIMD simulation results presented direct evidence that ¹O₂ could readily form through the pathway of O₂···O₂[−]¹O₂. And meanwhile, it could be further identified there was an *HO₂[−] transition state in the reaction of O₂ activation to ·O₂[−]. What's more, the CoFe-LDH was indeed an appreciable catalyst for diagnostic ¹O₂ specie generation.

3.2. Static DFT calculation for ROS evolution pathway

To tune the appropriate and efficient LDH catalysts, the free energy change, rate-determining step and intrinsic charge transfer in the ROS generation reaction should also be investigated. As exhibited in AIMD simulations, CoFe-LDH-based function cathodes were comprehensively investigated as Hetero-EF catalysts, the various LDH fingerprint dependence of different catalytic performances and degradation properties implied that distinct CoFe-LDH could have different catalytic reactivity and electronic structure. In addition, the ¹O₂ productions, catalytic performances and drug decay rates of LDH might be tuned by transition metal atomic ratio and structure estimating from the representational removal and characterization properties. The well-documented atomistic structure and the adoption of the identical CoFe-LDH moiety by different metals ratio proposed us an ideal model system to recognize the effects of the metal fingerprint in determining the generation of ¹O₂ and the catalytic activity (both theoretically and experimentally), which could provide a justifiable verification of the decontamination performance of the NFXN using CoFe-LDH catalysts.

For this reason, DFT calculations and AIMD were employed to explore CoFe-LDH as sustained ROS forming catalysts and affirm the roles of metal fingerprints in affecting the electronic nature of the atomic sites and consequently the ROS evolution reaction energetics. Conformed to previous work [51–54], the work speculated two potential ROS evolution reaction pathways that (I) proceeds *O₂, *O₂[−] and ¹O₂; (II) proceeds *H₂O₂ and *OH (the asterisk indexes the adsorption site).

As suggested by previous DFT calculations by us and others, [18] the O atoms next to M (M = Fe or Co atoms) and metal atoms in LDH catalysts could be the prioritized reactive sites for the oxygen and its intermediates (Pathway I). Thus, it could be considered that both the M and O atoms in CoFe-LDH catalysts as possible binding sites for the reactants. For the second pathway for OH formation in the Haber-Weiss circle, the preferential absorption sites could be the metal sites with Co, Fe atom whose absorption energies are different in these two sites.

Scheme 1. The pathway of ·O₂[−] and ¹O₂ generation: It could be conjectured and simulated that the O atoms could participate in the ¹O₂ evolution reaction process [55,56]. Because of stronger binding energy on O atoms than that on M atoms, the reactants and its intermediates prefer to bind at the O site other than the M sites and therefore the reaction proceeds through the single-site mechanism (Fig. S3).

The calculated energy diagrams of the ·O₂[−] and ¹O₂ evolution at pH = 7 for the different fingerprints of CoFe-LDH following the recommended reaction schemes were depicted in Fig. 2. The rate-determining

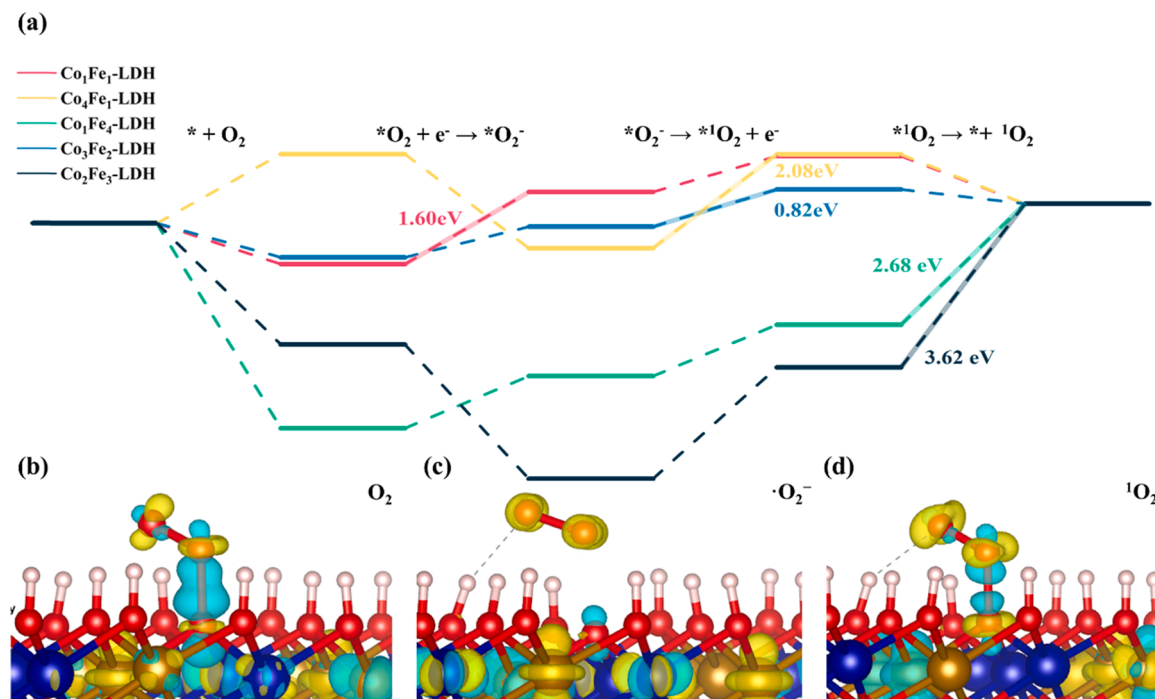


Fig. 2. (a) Free energy diagram for the pathway of $\cdot\text{O}_2$ and ${}^1\text{O}_2$ generation over CoFe-LDH. The highlights indicate the rate-determining step with the values of the limiting energy barrier labeled. (b-d) Calculated electron density differences ($\delta\rho = \rho_{A+B} - \rho_A - \rho_B$) of ${}^1\text{O}_2$ generation pathway on $\text{Co}_3\text{Fe}_2\text{-LDH}$ (cyan stands for holes and yellow for electrons).

step (RDS) was indexed to evaluate the limiting reaction barrier which is one non-negligible factor for determining the catalytic activity. For $\text{Co}_1\text{Fe}_4\text{-LDH}$ and $\text{Co}_2\text{Fe}_3\text{-LDH}$, the RDS was the desorption process of singlet oxygen with the reaction barrier as large as 2.68 eV and 3.62 eV. For $\text{Co}_1\text{Fe}_1\text{-LDH}$, the RDS was the process of $\cdot\text{O}_2$ to $*\text{O}_2^-$ with a much lower reaction barrier of 1.60 eV. The RDS of $\text{Co}_3\text{Fe}_2\text{-LDH}$ and $\text{Co}_4\text{Fe}_1\text{-LDH}$ catalytic reaction for ${}^1\text{O}_2$ formation was the oxidation of $*\text{O}_2^-$ towards $*{}^1\text{O}_2$ with 0.82 eV and 2.08 eV. The $\text{Co}_3\text{Fe}_2\text{-LDH}$ catalysis presented the smallest energy barrier of 0.82 eV with the generation of $*{}^1\text{O}_2$.

For comparison, calculations operated on the CoFe-LDH moieties for producing ${}^1\text{O}_2$ at pH = 7 showed the catalytic activity trend remained $\text{Co}_3\text{Fe}_2\text{-LDH} > \text{Co}_1\text{Fe}_1\text{-LDH} > \text{Co}_4\text{Fe}_1\text{-LDH} > \text{Co}_1\text{Fe}_4\text{-LDH} > \text{Co}_2\text{Fe}_3\text{-LDH}$ (Fig. 2). Our simulation results indicated that the catalytic activity and reaction pathways are strongly dependent on the metal fingerprints of CoFe-LDH. Moreover, in the aqueous solution, dissolved oxygens, superoxide radicals could also be induced by $\cdot\text{OH}$ released from Haber-Weiss circle to yield ${}^1\text{O}_2$.

Scheme 2. The pathway of $\cdot\text{OH}$ generation: On the other hand, for the pathway of the $\cdot\text{OH}$ generation, the mechanism should be attributed to Haber-Weiss circle. Hence, $*\text{H}_2\text{O}_2$ and $*\text{OH}$ should favorably reside and adsorb on the M atom (Fig. S4). According to the Haber-Weiss circle for Hetero-EF reaction, the free energy diagram of different CoFe-LDH fingerprints for producing $\cdot\text{OH}$ have also been investigated in Fig. S5. The RDS of all catalysts were listed in Table S3. Because of bimetallic hydroxide, Co atoms and Fe atoms are both optional active sites for Haber-Weiss reaction to create hydroxyl radicals. The smallest reaction barrier was 3.45 eV for Fe sites in $\text{Co}_3\text{Fe}_2\text{-LDH}$, which were almost higher than that for ${}^1\text{O}_2$ generation. This is to say that, in the LDH-based catalysis, the ${}^1\text{O}_2$ generation reaction could be more likely to proceed spontaneously than that for $\cdot\text{OH}$ formation at pH = 7.

To investigate the charge transfer in the process of the ${}^1\text{O}_2$ generation in the Heterogenous EF reaction, the electron density difference was computed in Fig. 2b-d. Along with theoretical graphs that the electron-donating from LDH catalysts to the ROS, assigned to the activation of O_2 , $\cdot\text{O}_2$ during the ROS evolution reaction, it could be identified that the

electron reapportion and significant charge transfer between the LDH and oxygen groups could be observed, which improved the catalytic performance toward the ROS evolution reaction. The charts of charges in LDH-O_2 , LDH-O_2^- and $\text{LDH-}{}^1\text{O}_2$ depicted that the electrons donated from the metal atoms (Fe or Co atoms on the surface of LDH catalysts) to the ROS species (O_2 , $\cdot\text{O}_2$ and ${}^1\text{O}_2$), significant density increasing occurred between the Co, Fe, and O atoms. Thus, the Fe and Co atoms in LDH catalysts could conduct as feasible electron donors populating the oxygen groups and its O (p) states, which could demonstrate the catalytic efficacy of the LDH catalysts. The Bader Charge Analysis unveiled that the charges directly migrated to oxygen species, namely 0.27 |e|, 1.30 |e| and 0.86 |e| coincided with the charge density analysis (Table S4) [57–59].

In light of the simulations, mechanisms and analysis, LDH catalysts could be directionally fabricated and tuned for practical decontamination of refractory organic matters, which could be a well-documented guideline, efficient, low-costly and environmentally friendly.

3.3. NFXN degradation and ROS generation performance

3.3.1. Catalysts fabrication and properties of the different fingerprints CoFe-LDH catalysts

Based on the dynamic-static DFT calculations, an appreciable tune strategy for LDH catalysts inducing ROS production on pollutants degradation was proposed. In the current work, the synthesis process and the formation of CoFe-LDH are illustrated in *Supplementary material*. CoFe-LDH with 5 different element ratios Co_1Fe_1 , Co_1Fe_4 , Co_2Fe_3 , Co_3Fe_2 , and Co_4Fe_1 were prepared by a mild solvothermal method using mother solution with $\text{Co}(\text{NO}_3)_2 \cdot 6 \text{ H}_2\text{O}$, $\text{Fe}(\text{NO}_3)_3 \cdot 9 \text{ H}_2\text{O}$, urea and ammonium fluoride dissolved in ultrapure water.

To affirm the surface elemental composition and valence states, the X-ray Photoelectron Spectroscopy (XPS) measurement and analysis were employed on Co_1Fe_1 , Co_1Fe_4 , Co_2Fe_3 , Co_3Fe_2 , and Co_4Fe_1 -LDHs (Fig. 3). XPS was discerned to affirm the elemental composition and chemical state of the sample surface to a certain extent. The high-resolution Fe 2p XPS spectrum of CoFe-LDH could be indexed into six peaks, as shown in

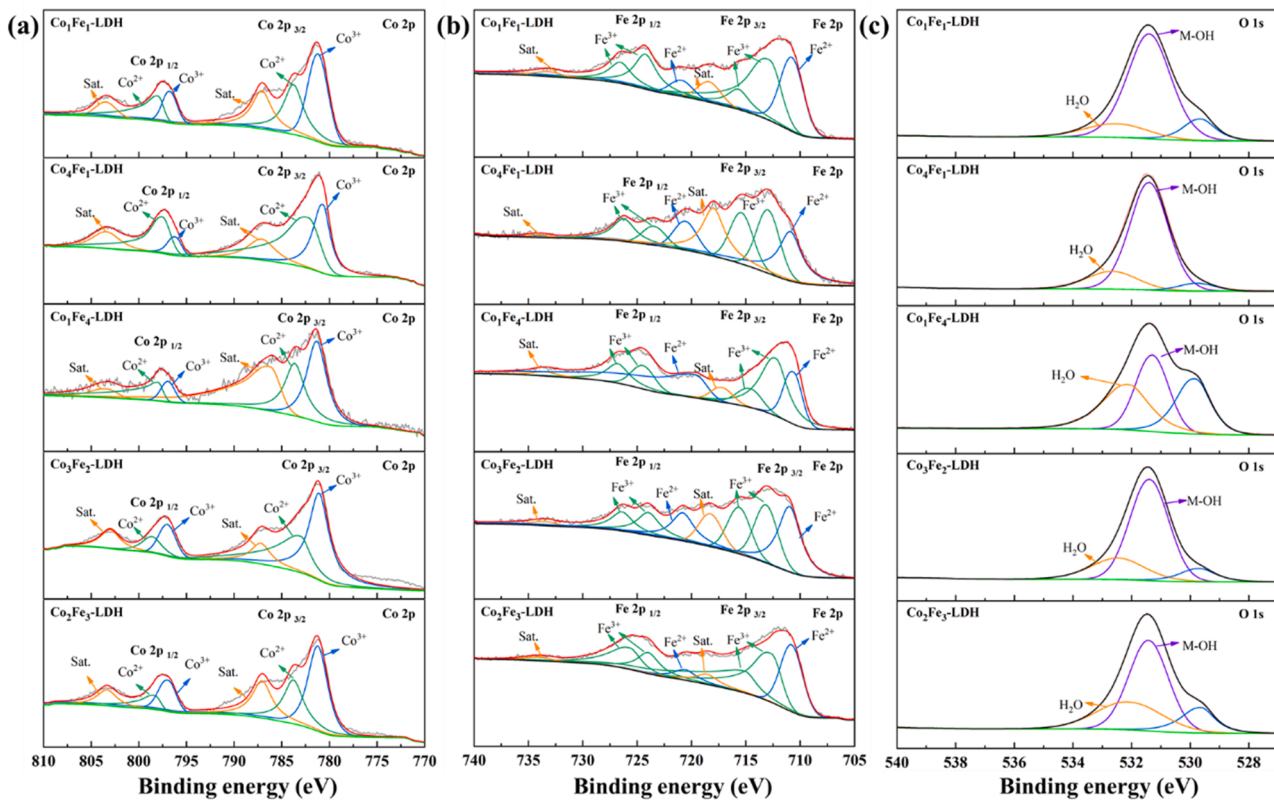


Fig. 3. XPS spectra of (a) Co 2p, (b) Fe 2p, and (c) O 1s of Co₁Fe₁, Co₁Fe₄, Co₂Fe₃, Co₃Fe₂, and Co₄Fe₁-LDHs.

Fig. 3, and the peaks at 733.52 ± 0.5 and 717.86 ± 0.7 eV are satellite peaks. The peaks at 720.30 ± 0.6 eV and 710.79 ± 0.2 eV are assigned to Fe^{2+} 2p_{3/2} and Fe^{2+} 2p_{1/2}, respectively, and the peaks at 712.69 ± 0.6 , 715.12 ± 0.7 , 724.22 ± 0.3 and 726.24 ± 0.6 eV belong to Fe^{3+} 2p_{1/2} and Fe^{3+} 2p_{3/2}, respectively. The Co 2p XPS spectra are exhibited in Fig. 3a, during the hydrothermal preparation of CoFe-LDH, the oxidation ability of Fe^{3+} and O_2 are able to promote the formation of Co^{3+} on the surface of CoFe-LDH, which is also conducive to the formation of chemical bonds at the interface. The Co 2p orbitals suggested two main spin-orbit doublets which were ascribed as Co 2p_{3/2} and Co 2p_{1/2}, respectively [60]. The Co 2p_{3/2} was further divided into two peaks at around 781.0 ± 0.4 and 782.99 ± 0.8 eV which were the peak of Co^{2+} and Co^{3+} species, while other peaks at 796.59 ± 0.5 and 798.09 ± 0.6 eV were relevant to Co^{2+} and Co^{3+} in Co 2p_{1/2} [61]. The two pairs of spin-orbitals (Co 2p_{3/2} and Co 2p_{1/2}) verified the existence of Co^{3+} and Co^{2+} in the CoFe-LDH samples [62]. Moreover, two satellite peaks found at 787.07 ± 0.5 and 803.34 ± 0.3 eV could also be attributed to the shake-up peaks of Co 2p_{1/2} and Co 2p_{3/2} of CoFe-LDH catalysts [63], respectively. In Fig. 3c, the O 1s peak could be divided into two peaks. The energy at 531.36 ± 0.1 eV was the stronger peak distributed to the surface hydroxyl group of the metal center which represents M-OH group. The weaker peak at 532.37 ± 0.3 eV revealed the presence of H_2O molecules [64]. And the peak at 529.68 ± 0.1 eV was assigned as the NO_3^- . Here, the O 1s spectra results were correlated with typical LDH structures [65]. The functional cathode CoFe-LDH/CF and LDH catalysts are both fabricated by one-step hydrothermal method in a Teflon-lined autoclave. Therefore, the catalysts on the electrode are duplicate. The morphology of catalysts on the electrode was also exhibited in Fig. S15 and Fig. S16.

The XRD patterns of the 5 different element ratios Co₁Fe₁, Co₁Fe₄, Co₂Fe₃, Co₃Fe₂, and Co₄Fe₁ Hetero-catalysts are depicted in Fig. S6a. As shown in Fig. S6a, prominent diffraction peaks of the samples could be obviously found at a series of reflections at 2θ values of 11.7° , 23.5° , 34.6° , 34.2° , and 46.8° , corresponding to (003), (006), (009), (101), and

(018), respectively [38,66,67]. The SEM in Fig. S7 presented the diagnostic flower-like and urchin-like structures of LDH catalysts. The results of XRD and SEM analysis jointly affirm that diverse fingerprints CoFe-LDH has been successfully synthesized. From the morphological and structural characterization studies in Fig. 3, Fig. S6a and Fig. S7, it was confirmed that 3D marigold flower-like CoFe-LDH electrocatalysts with 2D ultrathin nanosheets were successfully prepared by a one-step hydrothermal method.

Similarly, in order to further verify the different transition metal ratios of synthetic LDHs catalysts were tested by Inductively Coupled Plasma Atomic Emission Spectrometer (ICP) and the analytic results are depicted in the Table S1. The results in the Supplementary material clearly show that the different fingerprints CoFe samples maintained the molar ratios of experimental value and were prepared successfully.

Furthermore, the EIS analysis was performed to explore the charge-transfer resistance phenomena between CoFe-LDH and electrolyte interface. Fig. S6b shows the Nyquist plots for Co₁Fe₁, Co₁Fe₄, Co₂Fe₃, Co₃Fe₂, and Co₄Fe₁. In the circuit, R_s corresponds to the solution resistance, R_{ct} represents the charge transfer resistance (Table S2), and CPE denotes the electrochemical double layer capacity (C_{dl}). This result further confirms that Co₃Fe₂-LDH exhibits the lowest resistance (R_{ct}) value and a fast charge transfer rate due to more active sites leading to its enhanced performance.

3.4. Hetero-EF performance of CoFe-LDH catalysts

The previous studies elucidated that LDH could be pursued as a robust heterogenous-catalysts to significantly facilitate the yield of radicals and the abatement of pharmaceuticals in acidic water matrices [18]. To entirely penetrate the performance of CoFe-LDH in forming reactive oxygen species and its correlation with the fingerprint of heterogeneous catalysts, a batch of experiments on the removal of norfloxacin in wide pH tolerance have been carried out. The consumption efficacy of NFXN affirmed that the inherent adsorption of the drug by the

functional cathodes could be a small fraction which was less than 1%.

The acid-base value might be served as one of the most sensitive parameters in a Fenton process. Therefore, the effect of the pH value on heterogeneous catalysis was also indicated, which could shed new light on the influence of catalyst fingerprint on the efficiency of contaminants as well as the formation of ROS. CoFe-LDH displayed well-documented pH universality, depicting analogous organic compounds purification ability at pH = 3, 7, 9. In addition, the degradation activity of the $\text{Co}_3\text{Fe}_2\text{-LDH}$ and $\text{Co}_2\text{Fe}_3\text{-LDH}$ outperformed other LDH catalysts, which could be over 90% for total organic carbon (TOC) removal rate within 6 h in all mentioned pH values. All these appearances were also attributed to be one of the irreplaceable merits of this heterogeneous Fenton system compared to the conventional Fenton process.

Astonishingly, $\text{Co}_3\text{Fe}_2\text{-LDH}$ exhibited a 100% decontamination rate of NFXN within 20 min in neutral solution shown in Fig. 4e, which is comparatively higher than that of all previously mentioned LDH samples with differed element fingerprints while it could also be observed in the TOC removal reaction with a more appreciable decay performance. This difference in the achievement of catalysts validated by physical or chemical methods would be a point of concern and discussion, indicating that the fingerprints of catalysts could be assigned as the importance of pivotal in the Fenton reaction.

3.5. Spatiotemporal distribution of ROS from CoFe-LDH-based catalysis

To ascertain the oxidation mechanism of the LDH-catalytic Hetero-Fenton reaction for the decomposition of NFXN in a neutral aqueous solution, the measurement of ROS generated during the process was primarily required. It has been identified that the homogeneous Fenton reaction could release $\cdot\text{OH}$, as well as $\cdot\text{O}_2^-$ and ${}^1\text{O}_2$ [68–70]. Different from the Electron Spin Resonance (ESR) results under acidic conditions [71–73], it was difficult to detect the $\cdot\text{OH}$ signal in these LDH-reactions in a neutral buffer solution (Fig. S9), which verified that negligible $\cdot\text{OH}$ was formed in the systems. On the other hand, singlet oxygen (${}^1\text{O}_2$) was first detected with merely Na_2SO_4 background electrolyte. ESR spectra

(Fig. 5a) exhibited that 2,2,6,6-tetramethylpiperidine (TEMP) was the most popular ROS capture agent for ${}^1\text{O}_2$, which could produce 2,2,6,6-tetramethyl-4-piperidinol-N-oxyl (TEMPO) with typical triplet signal (1:1:1, a(N) = 16.9 G). As seen in Fig. 5, the chosen catalysts showed the discrepant intensity of the TEMPO signal which could also reflect the concentration of the ${}^1\text{O}_2$ yielded from mentioned CoFe-LDH with different structures and elements fingerprints. $\text{Co}_1\text{Fe}_4\text{-LDH}$ catalyst presented a pronounced decrease of ${}^1\text{O}_2$ compared with other CoFe-LDH. $\text{Co}_1\text{Fe}_1\text{-LDH}$, $\text{Co}_2\text{Fe}_3\text{-LDH}$ and $\text{Co}_4\text{Fe}_1\text{-LDH}$ catalysts could generate the similar quantity of ${}^1\text{O}_2$. Interestingly, $\text{Co}_3\text{Fe}_2\text{-LDH}$ -based Fenton system displayed the peak intensity signal among the catalysts system, which was corresponding to performance of NFXN and TOC elimination in Fig. 4.

The mechanism of LDH-based catalytic reaction and the molecules conversion of reactive species determined the removal observation of pharmaceuticals. Hence, more physicochemical activation strategies should be employed to investigate the intrinsic characteristics of the Hetero-Fenton system. In this work, probe detections were engaged in demonstrating reactive species in neutral reaction conditions. ${}^1\text{O}_2$ production was confirmed by the degradation of selective probe furfuryl alcohol (FFA) probe [74], whose second-order rate constant with ${}^1\text{O}_2$ is reported to be $1.2 \times 10^8 \text{ M}^{-1} \text{ s}^{-1}$ assigned highly selective to ${}^1\text{O}_2$. After 2 h FFA probe reaction (Fig. 5c), over 90% degradation of FFA (100 μM) could be obtained in all 5 LDH-based catalytic hetero-reaction. The removal rates of $\text{Co}_3\text{Fe}_2\text{-LDH}$ and $\text{Co}_2\text{Fe}_3\text{-LDH}$ notably reached 98.09% and 97.91%, respectively. After adding ethanol (50 mM) in the FFA reaction solution, a slight decrease (no more than 10%) was corroborated in Fig. 5d.

In addition, hydroxyl radicals [75] were hardly detected with only 4.0–9.5 μM in the system (Fig. S9b) probed by Terephthalic acid/2-hydroxyterephthalic acid (TPA/hTPA). However, based on Fig. 5d, after adding MeOH into the reactor, the degradation rate of FFA slightly still declined, which could be deduced that $\cdot\text{OH}$ reacted with hydrogen peroxide to form $\cdot\text{O}_2^-$ which is also a common by-product of the Haber-Weiss circle (Eq. (1)). Subsequently, the $\cdot\text{O}_2^-$ was also able to

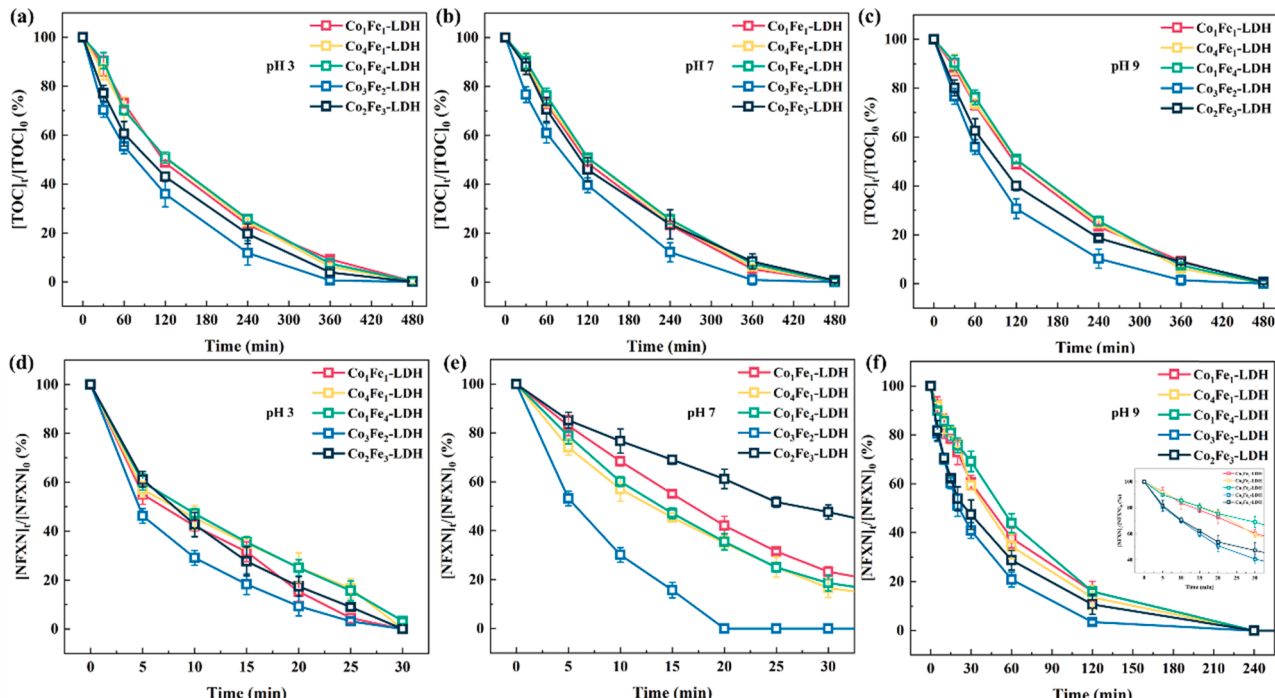


Fig. 4. (a-c) TOC mineralization efficiency of different catalysts at pH 3, 7, 9; (d-f) NFXN degradation behavior of different catalysts at pH 3, 7, 9. The inset figure in Fig. 4f is the NFXN decomposition process in 0–30 min at pH 9, which is also showed in Fig. S8. $[\text{NFXN}]_0 = 32 \text{ mg/L}$. The applied current was 50 mA provided by NAPUI single power supply (NAPUI, China).

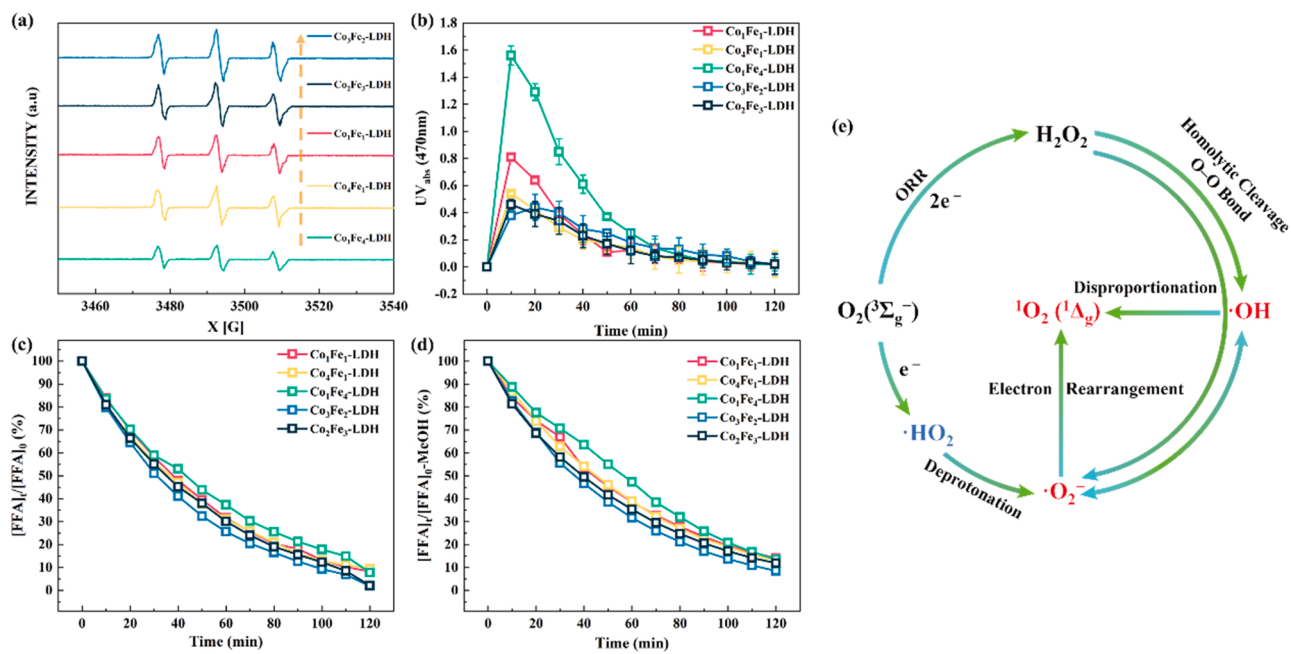
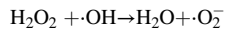


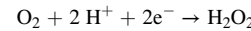
Fig. 5. (a) ESR spectra of TEMP- $^1\text{O}_2$ adducts formed in LDH-based Heterogeneous-EF process under neutral pH conditions, [TEMP]= 50 mM. (b) Determination of $\cdot\text{O}_2^-$ by using 100 μM XTT as a probe. (c) Investigation of $^1\text{O}_2$ by using 100 μM FFA. (d) Investigation of $^1\text{O}_2$ by using 100 μM FFA and 50 mM ethanol. (e) Production mechanisms of active species.

convert to $^1\text{O}_2$.



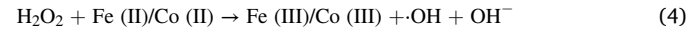
(1)

2e^- transfer ORR,



(3)

ii) **The Haber-Weiss Reaction between $\cdot\text{O}_2^-$, $\cdot\text{OH}$ and H_2O_2 .**
 H_2O_2 is decomposed into $\cdot\text{OH}$ (Eq. (4)).



(4)



(5)



(6)



(7)

According to the ESR and probe tests, the hydroxyl radicals, rarely converted to other species [77–79], are catalyzed to superoxide radicals via the Haber-Weiss circle, which are the dominant precursors of the singlet oxygen.

iii) $\cdot\text{O}_2^-$ Generation in Oxygen Pathway.

On the other pathway, O_2 obtains an electron to form $\cdot\text{O}_2^-$ at the cathode interface (Eq. (8)). And actually, based on the AIMD simulation in Section 3.2, The $\cdot\text{HO}_2$ is found as a transition state matter in the process. The hydroperoxyl radical gives rise to the superoxide radical when it loses a proton (Eq. (9)).



(8)



(9)

iv) $^1\text{O}_2$ Generation Pathway.

Finally, $\cdot\text{O}_2^-$ can converted to $^1\text{O}_2$ reacted with $\cdot\text{OH}$ through Eq. (10).



(10)

In our work, although the $\cdot\text{O}_2^-$ might be the only precursor for $^1\text{O}_2$, yet there is also a disproportionation reaction (Eq. (11)) producing $^1\text{O}_2$ which could be formed from $\cdot\text{OH}$ in the previous research.[80].



(11)

3.6. $^1\text{O}_2$ Formation mechanism in the LDH-based hetero-EF reaction

Benefiting from the continuous production of ROS, a feasible pathway for $\cdot\text{O}_2^-$ and $^1\text{O}_2$ generation was presented (Fig. 5e). $\cdot\text{O}_2^-$ is the indispensable active precursor for the $^1\text{O}_2$ formation and its production paths could be separated into:

i) Oxygen Reduction Reaction for H_2O_2 generation.

First, O_2 is reduced to form H_2O_2 (Eq. (3)) at the cathode interface via

3.7. Machine learning model for potent catalysts screening and selecting

According to the simulations and experiments, it has been demonstrated that the fingerprint of materials including stoichiometric ratio, elemental property statistics, and electronic structure attributes potentially impacted the decontamination performance, the yield and types of ROS. Yet unfortunately, the intrinsic relationship between the fingerprint characteristics of catalysts and pollutant degradation quantitatively was hard to figure out. Hence, it is necessary to bridge the physicochemical activation properties and practical engineering catalysts screening using booming machine learning model, a black-box model, laconically and efficiently.

Model training and performance: In the work, Linear Regression (LR), Gradient Boosting Regressor (GBR) and Random Forest Regressor (RFR) algorithms were employed to build prediction models for comparing and obtaining the most reliable models. The algorithm was depicted in Fig. S12. On the other hand, considering the limited data in this work and related research in this area [81,82], Monte Carlo cross validation [83,84] was used to select an appropriate machine learning algorithm for this work. The fold of cross-validation was 10, which randomly divided the data into 10 parts, trained models on 9 parts and aimed to predict the features of the remaining set [43].

Simultaneously, excessive features would cause redundant problems, and inadequate features could not meet the specific demands of model building. Thus, in order to optimize the feature set, several features (created from Magpie) without contribution had been removed, we gained the final feature set. After the pre-optimization of the data, the models have been shown in Fig. 6, the highest prediction accuracy of $r^2 = 0.940$ gained by the GBR algorithm among the 3 algorithms. Other models exhibited inferior accuracy for predicting the degradation rate of the drug. RFR model has achieved a very close coefficient ($r^2 = 0.925$). LR model had unsatisfied prediction performances due to its low $r^2 = 0.476$ score. Comparison Pearson correlation coefficient heat maps are also shown in Fig. S14 in Supplementary Information to reflect the potential relationship of the fingerprint features and the degradation rate each other. Each small square's color in the heat maps showed the correlation of each feature pair. So far, after training by the GBR algorithm, a credible prediction model for potent catalysts based on their material fingerprint nature was obtained, which would be efficient for searching novel catalysts on NFXN degradation reaction. The prediction model had also been tested by using practical catalysts in Fig. S13, which were consistent with the experimental degradation rate for NFXN.

All these predictions have been confirmed that the catalysts' fingerprint features could have a significant effect on its catalysis efficiency of drug degradation and ROS species generation. What's more, ML-assisted materials design strategy with higher efficacy, shorter time and lower cost could also address some shortcomings of traditional

experimental selection. Our findings enrich the fundamental understanding of catalysts screening and optimization, which will be useful for the application of Hetero-EF processes.

4. Conclusion

A novel Simulation-Experiment-Prediction framework has been creatively and successfully proposed to reveal the atomic-level mechanisms of ROS evolution reactions and to screen the robust catalysts for Hetero-EF reaction. Static-dynamic DFT calculations have unveiled atom-level ROS evolution mechanisms and proposed a feasible strategy for LDH catalysts fabrication and tuning. The optimal catalyst is $\text{Co}_3\text{Fe}_2\text{-LDH}$ with the lowest free energy barrier of RDS and confirm the conversion pathways of the predominant $^1\text{O}_2$. An exclusive $^1\text{HO}_2$ transition state was also identified in the process of reactive oxygen species. Subsequently, CoFe-LDH catalysts have been experimentally tuned, optimized and pursued as an efficient activator of singlet oxygen, in which $\text{Co}_3\text{Fe}_2\text{-LDH}$ exhibited the best catalysis performance as well as the quantity of the ROS concentration than other catalysts, which prove validity of theories and successfully select the optimal catalysts for drug removal based on the brilliant performance of NFXN degradation and ROS evolution. After obtaining the database from experiments, calculations and previous works, a GBR prediction model has been established employing the machine learning algorithm for exploring complicated and appreciable catalysts on the drug elimination based on catalysts' fingerprint features, which is low-cost, efficient and accurate. This sustainable, flexible and scalable approach of Hetero-EF has boomerang potential in diverse applications, including environmental catalysis, environmental remediation, and real wastewater purification. Moreover, it could be envisioned that the established GBR model would also be optimized and promoted with more valuable contaminants degradation and catalysis data achieved from diverse environmental research. Our findings will pave the way for future smarter research and design strategies for low-cost, efficient and convenient environmental process mechanism exploration and catalysts screen.

CRediT authorship contribution statement

Dehai Yu: Conceptualization, Methodology, Validation, Formal analysis, Investigation, Writing – original draft, Writing – review & editing; **Fei Wu:** Resources, Investigation; **Junguo He:** Funding acquisition, Supervision. **Langming Bai:** Writing – review & editing; **Yanshi Zheng:** Data curation. **Ziyao Wang:** Data curation. **Jie Zhang:** Funding acquisition.

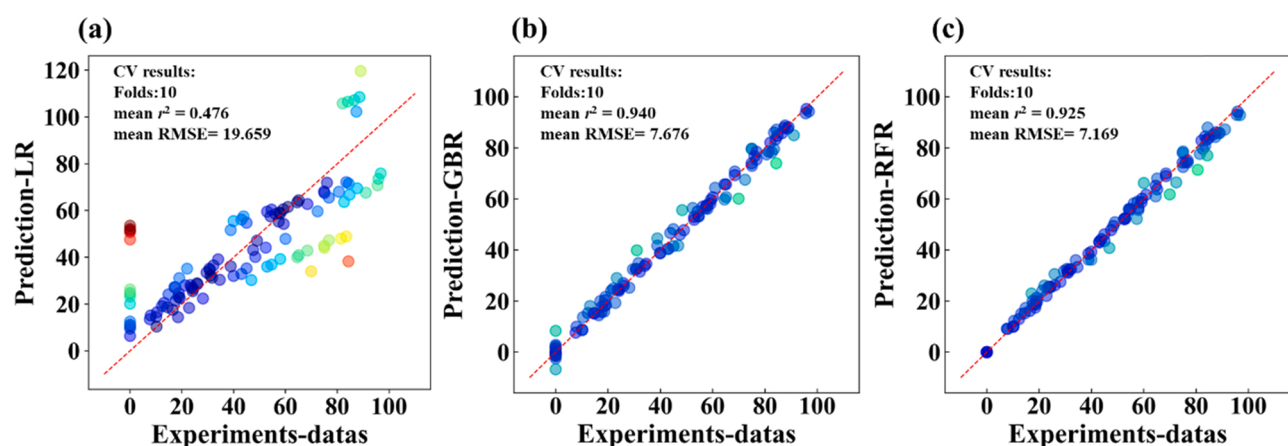


Fig. 6. Prediction performance of other models trained by different ML methods: (a) LR, (b) GBR, (c) RFR.

Declaration of Competing Interest

The authors declare that they have no known competing financial interests or personal relationships that could have appeared to influence the work reported in this paper.

Data Availability

Data will be made available on request.

Acknowledgments

This work was supported by the National Natural Science Foundation of China (No. 52170029), Heilongjiang Postdoctoral Fund (LBHTZ2110), and Heilongjiang Touyan Innovation Team Program (HIT-SE-01). The authors would like to thank the Shiyanjia Lab (www.shiyanjia.com) for the measurement of XPS.

Appendix A. Supporting information

Supplementary data associated with this article can be found in the online version at [doi:10.1016/j.apcatb.2022.121880](https://doi.org/10.1016/j.apcatb.2022.121880).

References

- [1] X. Liu, J.C. Steele, X.Z. Meng, Usage, residue, and human health risk of antibiotics in Chinese aquaculture: a review, *Environ. Pollut.* 223 (2017) 161–169.
- [2] X. Liu, Y. Zhou, J. Zhang, L. Luo, Y. Yang, H. Huang, H. Peng, L. Tang, Y. Mu, Insight into electro-Fenton and photo-Fenton for the degradation of antibiotics: mechanism study and research gaps, *Chem. Eng. J.* 347 (2018) 379–397.
- [3] W. Giger, A.C. Alder, E.M. Golet, H.P.E. Kohler, C.S. Mcardell, E. Molnar, H. Siegrist, J.F. Suter, Occurrence and fate of antibiotics as trace contaminants in wastewater, sewage sludges, and surface waters, *Chim. Int. J. Chem.* 57 (2003) 485–491.
- [4] E.M. Golet, A.C. Alder, W. Giger, Environmental exposure and risk assessment of fluoroquinolone antibacterial agents in wastewater and river water of the glatt valley watershed, Switzerland, *Environ. Sci. Technol.* 36 (2002) 3645–3651.
- [5] E. Mousset, W.H. Loh, W.S. Lim, L. Jarry, Z.X. Wang, O. Lefebvre, Cost comparison of advanced oxidation processes for wastewater treatment using accumulated oxygen-equivalent criteria, *Water Res.* 200 (2021).
- [6] H. Olvera-Vargas, J. Dubuc, Z.X. Wang, L. Coudert, C.M. Neculita, O. Lefebvre, Electro-Fenton beyond the degradation of organics: treatment of thiosalts in contaminated mine water, *Environ. Sci. Technol.* 55 (2021) 2564–2574.
- [7] H. Olvera-Vargas, Z.X. Wang, J.X. Xu, O. Lefebvre, Synergistic degradation of GenX (hexafluoropropylene oxide dimer acid) by pairing graphene-coated Ni-foam and boron doped diamond electrodes, *Chem. Eng. J.* 430 (2022).
- [8] J.J. Hu, S. Wang, J.Q. Yu, W.K. Nie, J. Sun, S.B. Wang, Duet Fe3C and FeNx Sites for H2O2 generation and activation toward enhanced electro-fenton performance in wastewater treatment, *Environ. Sci. Technol.* 55 (2021) 1260–1269.
- [9] C.A. Martinez-Huiti, M.A. Rodriguez, I. Sires, O. Scialdone, Single and coupled electrochemical processes and reactors for the abatement of organic water pollutants: a critical review, *Chem. Rev.* 115 (2015) 13362–13407.
- [10] M.A. Oturan, J.-J. Aaron, Advanced oxidation processes in water/wastewater treatment: principles and applications, a review, *Crit. Rev. Environ. Sci. Technol.* 44 (2014) 2577–2641.
- [11] Y. Yao, Y. Pan, Y. Yu, Z. Yu, L. Lai, F. Liu, L. Wei, Y. Chen, Bifunctional catalysts for heterogeneous electro-Fenton processes: a review, *Environ. Chem. Lett.* (2022).
- [12] H. Lan, J. Li, M. Sun, X. An, C. Hu, R. Liu, H. Liu, J. Qu, Efficient conversion of dimethylarsinate into arsenic and its simultaneous adsorption removal over FeCx/N-doped carbon fiber composite in an electro-Fenton process, *Water Res.* 100 (2016) 57–64.
- [13] V. Poza-Nogueiras, E. Rosales, M. Pazos, M.Á. Sanromán, Current advances and trends in electro-Fenton process using heterogeneous catalysts – a review, *Chemosphere* 201 (2018) 399–416.
- [14] H. Bataineh, O. Pestovsky, A. Bakac, pH-induced mechanistic changeover from hydroxyl radicals to iron(IV) in the Fenton reaction, *Chem. Sci.* 3 (2012) 1594–1599.
- [15] Q. Yi, J. Ji, B. Shen, C. Dong, J. Liu, J. Zhang, M. Xing, Singlet oxygen triggered by superoxide radicals in a molybdenum cocatalytic fenton reaction with enhanced REDOX activity in the environment, *Environ. Sci. Technol.* 53 (2019) 9725–9733.
- [16] Y. Zong, X. Guan, J. Xu, Y. Feng, Y. Mao, L. Xu, H. Chu, D. Wu, Unraveling the overlooked involvement of high-valent cobalt-oxo species generated from the Cobalt(II)-activated peroxymonosulfate process, *Environ. Sci. Technol.* 54 (2020) 16231–16239.
- [17] Q. Yan, C. Lian, K. Huang, L. Liang, H. Yu, P. Yin, J. Zhang, M. Xing, Constructing an acidic microenvironment by MoS2 in heterogeneous fenton reaction for pollutant control, *Angew. Chem. -Int. Ed.* 60 (2021) 17155–17163.
- [18] D.H. Yu, J.G. He, Z.Y. Wang, H.L. Pang, L. Li, Y.S. Zheng, Y.W. Chen, J. Zhang, Mineralization of norfloxacin in a CoFe-LDH/CF cathode-based heterogeneous electro-fenton system: preparation parameter optimization of the cathode and conversion mechanisms of H2O2 to center dot OH, *Chem. Eng. J.* 417 (2021).
- [19] M. Zafari, D. Kumar, M. Umer, K.S. Kim, Machine learning-based high throughput screening for nitrogen fixation on boron-doped single atom catalysts, *J. Mater. Chem. A* 8 (2020) 5209–5216.
- [20] S.M.N. Jeghan, J. Kim, G. Lee, Hierarchically designed CoMo marigold flower-like 3D nano-heterostructure as an efficient electrocatalyst for oxygen and hydrogen evolution reactions, *Appl. Surf. Sci.* 546 (2021).
- [21] A. Chen, X. Zhang, L. Chen, S. Yao, Z. Zhou, A machine learning model on simple features for CO₂ reduction electrocatalysts, *J. Phys. Chem. C* 124 (2020) 22471–22478.
- [22] I. Takigawa, K.-i Shimizu, K. Tsuda, S. Takakusagi, Machine-learning prediction of the d-band center for metals and bimetals, *RSC Adv.* 6 (2016) 52587–52595.
- [23] Y. Chen, C.J. Miller, T.D. Waite, pH dependence of hydroxyl radical, ferryl, and/or ferric peroxy species generation in the heterogeneous fenton process, *Environ. Sci. Technol.* (2021).
- [24] S. Sun, C. Shan, Z. Yang, S. Wang, B. Pan, Self-Enhanced Selective Oxidation of Phosphonate into Phosphate by Cu(II)/H2O2: Performance, Mechanism, and Validation, *Environmental Science & Technology*, (2021).
- [25] Z. Wang, W. Qiu, S.-Y. Pang, Q. Guo, C. Guan, J. Jiang, Aqueous Iron(IV)-Oxo Complex: An Emerging Powerful Reactive Oxidant Formed by Iron(II)-Based Advanced Oxidation Processes for Oxidative Water Treatment, *Environmental Science & Technology*, (2022).
- [26] T. Zhang, Y. Wen, Z. Pan, Y. Kuwahara, K. Mori, H. Yamashita, Y. Zhao, X. Qian, Overcoming acidic H2O2/Fe(II/III) redox-induced Low H2O2 utilization efficiency by carbon quantum dots fenton-like catalysis, *Environ. Sci. Technol.* 56 (2022) 2617–2625.
- [27] A. Chen, X. Zhang, Z. Zhou, Machine learning: accelerating materials development for energy storage and conversion, *InfoMat* 2 (2020) 553–576.
- [28] N.C. Frey, J. Wang, G.I. Vega Bellido, B. Anasori, Y. Gogotsi, V.B. Shenoy, Prediction of synthesis of 2D metal carbides and nitrides (mxenes) and their precursors with positive and unlabeled machine learning, *ACS Nano* 13 (2019) 3031–3041.
- [29] S. Lu, Q. Zhou, Y. Ouyang, Y. Guo, Q. Li, J. Wang, Accelerated discovery of stable lead-free hybrid organic-inorganic perovskites via machine learning, *Nature Communications* 9 (2018) 3405.
- [30] J. Im, S. Lee, T.-W. Ko, H.W. Kim, Y. Hyon, H. Chang, Identifying Pb-free perovskites for solar cells by machine learning, *npj Computational Materials* 5 (2019) 37.
- [31] A. Ali, H. Park, R. Mall, B. Aïssa, S. Sanvito, H. Bensmail, A. Belaïdi, F. El-Mellouhi, Machine learning accelerated recovery of the cubic structure in mixed-cation perovskite thin films, *Chem. Mater.* 32 (2020) 2998–3006.
- [32] M. Fernandez, P.G. Boyd, T.D. Daff, M.Z. Aghaji, T.K. Woo, Rapid and accurate machine learning recognition of high performing metal organic frameworks for CO₂ capture, *J. Phys. Chem. Lett.* 5 (2014) 3056–3060.
- [33] Y. He, E.D. Cubuk, M.D. Allendorf, E.J. Reed, Metallic metal–organic frameworks predicted by the combination of machine learning methods and Ab initio calculations, *J. Phys. Chem. Lett.* 9 (2018) 4562–4569.
- [34] Y. Wu, H. Duan, H. Xi, Machine Learning-driven insights into defects of zirconium metal–organic frameworks for enhanced ethane–ethylene separation, *Chem. Mater.* 32 (2020) 2986–2997.
- [35] X. Zhu, J. Yan, M. Gu, T. Liu, Y. Dai, Y. Gu, Y. Li, Activity origin and design principles for oxygen reduction on dual-metal-site catalysts: a combined density functional theory and machine learning study, *J. Phys. Chem. Lett.* 10 (2019) 7760–7766.
- [36] S.O. Ganiyu, T.X. Huong Le, M. Bechelany, N. Oturan, S. Papirio, G. Esposito, E. van Hullebusch, M. Cretin, A. Oturan, Electrochemical mineralization of sulfamethoxazole over wide pH range using FeIIFeIII LDH modified carbon felt cathode: degradation pathway, toxicity and reusability of the modified cathode, *Chem. Eng. J.* 350 (2018) 844–855.
- [37] S.O. Ganiyu, T.X. Huong Le, M. Bechelany, G. Esposito, E.D. van Hullebusch, M. A. Oturan, M. Cretin, A hierarchical CoFe-layered double hydroxide modified carbon-felt cathode for heterogeneous electro-Fenton process, *J. Mater. Chem. A* 5 (2017) 3655–3666.
- [38] Y. Wu, H. Wang, Y. Sun, T. Xiao, W. Tu, X. Yuan, G. Zeng, S. Li, J.W. Chew, Photogenerated charge transfer via interfacial internal electric field for significantly improved photocatalysis in direct Z-scheme oxygen-doped carbon nitrogen/CoAl-layered double hydroxide heterojunction, *Appl. Catal. B: Environ.* 227 (2018) 530–540.
- [39] G. Kresse, J. Furthmüller, Efficiency of ab-initio total energy calculations for metals and semiconductors using a plane-wave basis set, *Comp. Mat. er* 6 (1996) 15–50.
- [40] G. Kresse, F. J. Efficient iterative schemes for ab initio total-energy calculations using a plane-wave basis set, *Phys. Rev. B (Condens. Matter)* 54 (1996) 11169–11186.
- [41] J.P. Perdew, K. Burke, M. Ernzerhof, Generalized Gradient Approximation Made Simple [Phys. Rev. Lett. 77, 3865 (1996)], *Physical Review Letters*, (1997).
- [42] J. VandeVondele, M. Krack, F. Mohamed, M. Parrinello, T. Chassaing, J. Hutter, QUICKSTEP: fast and accurate density functional calculations using a mixed Gaussian and plane waves approach, *Comput. Phys. Commun.* 167 (2005) 103–128.
- [43] L. Ward, A. Agrawal, A. Choudhary, C. Wolverton, A general-purpose machine learning framework for predicting properties of inorganic materials, *npj Comput. Mater.* 2 (2016).

[44] J. Greeley, T.F. Jaramillo, J. Bonde, I. Chorkendorff, J.K. Nørskov, Computational high-throughput screening of electrocatalytic materials for hydrogen evolution, *Nat. Mater.* 5 (2006) 909–913.

[45] K. Tran, Z.W. Ulissi, Active learning across intermetallics to guide discovery of electrocatalysts for CO₂ reduction and H₂ evolution, *Nature, Catalysis* 1 (2018) 696–703.

[46] Y. Xiao, L.J. Miara, Y. Wang, G. Ceder, Computational screening of cathode coatings for solid-state batteries, *Joule* 3 (2019) 1252–1275.

[47] C. Clayton, Materials science and engineering: An introduction by W. D. Callister Jr.; published by Wiley, Chichester, West Sussex, 1985; 602 pp.; price, £40.40, *Materials Science and Engineering*, 94 (1987) 266–267.

[48] B. Meredig, A. Agrawal, S. Kirklin, J.E. Saal, J.W. Doak, A. Thompson, K. Zhang, A. Choudhary, C. Wolverton, Combinatorial screening for new materials in unconstrained composition space with machine learning, *Phys. Rev. B* 89 (2014).

[49] J.-C. Liu, Y. Tang, C.-R. Chang, Y.-G. Wang, J. Li, Mechanistic insights into propene epoxidation with O₂-H₂O mixture on Au₇/α-Al₂O₃: a hydroperoxyl pathway from ab initio molecular dynamics simulations, *ACS Catal.* 6 (2016) 2525–2535.

[50] G. Wang, The Structure and the Production of Singlet Oxygen, *Journal of Jiamusi University(Natural Science Edition)*, (1999).

[51] N. Macia, R. Bresoli-Obach, S. Nonell, B. Heyne, Hybrid silver nanocubes for improved plasmon-enhanced singlet oxygen production and inactivation of bacteria, *J. Am. Chem. Soc.* 141 (2019) 684–692.

[52] N. Mahne, B. Schafzahl, C. Leybold, M. Leybold, S. Grumm, A. Leitgeb, G. A. Strohmeier, M. Wilkening, O. Fontaine, D. Kramer, C. Slugovc, S.M. Borisov, S. A. Freunberger, Singlet oxygen generation as a major cause for parasitic reactions during cycling of aprotic lithium-oxygen batteries, *Nat. Energy* 2 (2017).

[53] H. Wang, X. Yang, W. Shao, S. Chen, J. Xie, X. Zhang, J. Wang, Y. Xie, Ultrathin black phosphorus nanosheets for efficient singlet oxygen generation, *J. Am. Chem. Soc.* 137 (2015) 11376–11382.

[54] Z. Zhou, J. Song, R. Tian, Z. Yang, G. Yu, L. Lin, G. Zhang, W. Fan, F. Zhang, G. Niu, L. Nie, X. Chen, Activatable singlet oxygen generation from lipid hydroperoxide nanoparticles for cancer therapy, *Angew. Chem. -Int. Ed.* 56 (2017) 6492–6496.

[55] Y. Dong, P. Zhang, Y. Kou, Z. Yang, Y. Li, X. Sun, A. First-Principles, Study of oxygen formation over nife-layered double hydroxides surface, *Catal. Lett.* 145 (2015) 1541–1548.

[56] S.-T. Zhang, H. Yan, M. Wei, D.G. Evans, X. Duan, Valence force field for layered double hydroxide materials based on the parameterization of octahedrally coordinated metal cations, *J. Phys. Chem. C* 116 (2012) 3421–3431.

[57] V. Wang, N. Xu, J.-C. Liu, G. Tang, W.-T. Geng, VASPKIT: a user-friendly interface facilitating high-throughput computing and analysis using VASP code, *Comput. Phys. Commun.* 267 (2021).

[58] Y.S. Wei, M. Zhang, R.Q. Zou, Q. Xu, Metal-organic framework-based catalysts with single metal sites, *Chem. Rev.* 120 (2020) 12089–12174.

[59] J.R. Yang, W.H. Li, D.S. Wang, Y.D. Li, Electronic metal-support interaction of single-atom catalysts and applications in electrocatalysis, *Adv. Mater.* 32 (2020).

[60] Z. Yang, Z. Chen, Y. Jiang, M. Chi, G. Nie, X. Lu, C. Wang, Palladium nanoparticles modified electrospun CoFe2O4 nanotubes with enhanced peroxidase-like activity for colorimetric detection of hydrogen peroxide, *RSC Adv.* 6 (2016).

[61] D. Lee, Q.X. Xia, R.S. Mane, J.M. Yun, K.H. Kim, Direct successive ionic layer adsorption and reaction (SILAR) synthesis of nickel and cobalt hydroxide composites for supercapacitor applications, *J. Alloy. Compd.* (2017). S0925838817321692.

[62] O.O. Balayeva, A.A. Azizo V, M.B. Muradov, R.M. Alosmanov, S. J. Mammadyarova, Cobalt chromium-layered double hydroxide, α- and β- Co(OH)₂ and amorphous Cr(OH)₃: synthesis, modification and characterization, *Heliyon* 5 (2019), e02725.

[63] L. Rong, C. Sun, L. Jia, Z. Qiang, Sulfur-doped CoFe2O4 nanopowders for enhanced visible-light photocatalytic activity and magnetic properties, *Rsc Adv.* 7 (2017).

[64] T. Bhowmik, M.K. Kundu, S. Barman, Cofe layered double hydroxide supported on graphitic carbon nitrides: an efficient and durable bi-functional electrocatalyst for oxygen evolution and hydrogen evolution reactions, *ACS Appl. Energy Mater.* (2018) *acsael.7b00305*.

[65] J. Du, Z. Zou, A. Yu, C. Xu, Selenization of NiMn-layered double hydroxide with enhanced electrocatalytic activity for oxygen evolution, *Dalton Transactions*, (2018) 10.1039/C1038DT01372A.

[66] H. Li, J. Li, C. Xu, P. Yang, D.H.L. Ng, P. Song, M. Zuo, Hierarchically porous MoS₂/CoAl-LDH/HCF with synergistic adsorption-photocatalytic performance under visible light irradiation, *J. Alloy. Compd.* 698 (2017) 852–862.

[67] Y.D.S. Zhang, TiO₂@ layered double hydroxide core-shell nanospheres with largely enhanced photocatalytic activity toward O₂ Generation, *Adv. Funct. Mater.* 25 (2015) 2243–2249.

[68] A. Babuponnusami, K. Muthukumar, A review on Fenton and improvements to the Fenton process for wastewater treatment, *J. Environ. Chem. Eng.* 2 (2014) 557–572.

[69] Y. Pan, H. Su, Y. Zhu, F.V. Molamahmood, M. Long, CaO₂ based Fenton-like reaction at neutral pH: ACCELERated reduction of ferric species and production of superoxide radicals, *Water Res.* 145 (2018) 731–740.

[70] H. Sugimoto, D.T. Sawyer, Iron(II)-induced activation of hydrogen peroxide to ferryl ion (FeO₂⁺) and singlet oxygen (1O₂) in acetonitrile: monoxygenations, dehydrogenations, and dioxygenations of organic substrates, *J. Am. Chem. Soc.* 106 (1984) 4283–4285.

[71] J. An, N. Li, Y. Wu, S. Wang, C. Liao, Q. Zhao, L. Zhou, T. Li, X. Wang, Y. Feng, Revealing decay mechanisms of H₂O₂-based electrochemical advanced oxidation processes after long-term operation for phenol degradation, *Environ. Sci. Technol.* 54 (2020) 10916–10925.

[72] Y. Yang, S. Qiao, J. Zhou, X. Quan, Mitigating membrane fouling based on in situ center dot OH Generation in a Novel Electro-Fenton Membrane Bioreactor, *Environ. Sci. Technol.* 54 (2020) 7669–7676.

[73] S. Zhang, M. Sun, T. Hettke, A. Deshmukh, X. Zhou, S. Weon, M. Elimelech, J.-H. Kim, Mechanism of heterogeneous fenton reaction kinetics enhancement under nanoscale spatial confinement, *Environ. Sci. Technol.* 54 (2020) 10868–10875.

[74] Y. Zhao, M. Sun, X. Wang, C. Wang, D. Lu, W. Ma, S.A. Kube, J. Ma, M. Elimelech, Janus electrocatalytic flow-through membrane enables highly selective singlet oxygen production, *Nat. Commun.* 11 (2020).

[75] Y. Zhu, F. Deng, S. Qiu, F. Ma, Y. Zheng, L. Gao, A self-sufficient electro-Fenton system with enhanced oxygen transfer for decontamination of pharmaceutical wastewater, *Chem. Eng. J.* 429 (2022).

[76] B. Liu, W. Guo, W. Jia, H. Wang, Q. Si, Q. Zhao, H. Luo, J. Jiang, N. Ren, Novel nonradical oxidation of sulfonamide antibiotics with Co(II)-Doped g-C₃N₄-activated peracetic acid: role of high-valent cobalt-oxo species, *Environ. Sci. Technol.* 55 (2021) 12640–12651.

[77] X. Li, J. Liu, A.I. Rykov, H. Han, C. Jin, X. Liu, J. Wang, Excellent photo-Fenton catalysts of Fe-Co Prussian blue analogues and their reaction mechanism study, *Appl. Catal. B-Environ.* 179 (2015) 196–205.

[78] Z. Yang, J. Qian, A. Yu, B. Pan, Singlet oxygen mediated iron-based Fenton-like catalysis under nanoconfinement, *Proc. Natl. Acad. Sci. USA* 116 (2019) 6659–6664.

[79] A.U. Khan, M. Kasha, Singlet molecular-oxygen in the haber-weiss reaction, *Proc. Natl. Acad. Sci. USA* 91 (1994) 12365–12367.

[80] P. Gao, Y. Song, M. Hao, A. Zhu, H. Yang, S. Yang, An effective and magnetic Fe₂O₃-ZrO₂ catalyst for phenol degradation under neutral pH in the heterogeneous Fenton-like reaction, *Sep. Purif. Technol.* 201 (2018) 238–243.

[81] J. Liu, W. Hu, M. Sun, O. Xiong, H. Yu, H. Feng, X. Wu, L. Tang, Y. Zhou, Enhancement of Fenton processes at initial circumneutral pH for the degradation of norfloxacin with Fe@Fe₂O₃ core-shell nanomaterials, *Environ. Technol.* 40 (2019) 3632–3640.

[82] G. Wang, D. Zhao, F. Kou, Q. Ouyang, J. Chen, Z. Fang, Removal of norfloxacin by surface Fenton system (MnFe₂O₄/H₂O₂): Kinetics, mechanism and degradation pathway, *Chem. Eng. J.* 351 (2018) 747–755.

[83] L.M. Hall, E. Frank, G. Holmes, B. Pfahringer, P. Reutemann, I.H. Witten, The WEKA data mining software, (2009).

[84] D.E. King, Dlib-ML: a machine learning toolkit, *J. Mach. Learn. Res.* 10 (2009) 1755–1758.